Electronically resonant third-order sum frequency generation spectroscopy using a nanosecond white-light supercontinuum

Hiroki Segawa,[1] Naoki Fukutake,[2] Philippe Leproux,[3] Vincent Couderc,[3] Takeaki Ozawa,[1] and Hideaki Kano[4,*]

[1]*Department of Chemistry, School of Science, The University of Tokyo, 7-3-1, Hongo, Bunkyo-ku, Tokyo,113-0033, Japan*
[2]*Core Technology Center, NIKON Corporation, 10-1, Asamizodai1-chome, Minami-ku, Sagamihara, Kanagawa, 252-0328, Japan*
[3] *Xlim Research Institute, CNRS-University of Limoges, 123 avenue Albert Thomas, 87060 Limoges cedex, France*
[4] *Institute of Applied Physics, University of Tsukuba, 1-1-1 Tennodai, Tsukuba, Ibaraki, 305-8573, Japan*
[*]*hkano@bk.tsukuba.ac.jp*

Abstract: Third-order sum frequency generation (TSFG) is one of the third-order nonlinear optical processes, and has the generation mechanism analogous to third harmonic generation (THG). By using a white-light supercontinuum, we can obtain broadband multiplex TSFG spectra. In the present study, we developed an electronically resonant TSFG spectrometer, and applied it to obtain TSFG spectra of hemoproteins. Analyzed TSFG ratio spectra clearly showed the resonant enhancement attributable to the electronic state of hemoproteins. This is a promising method for the imaging of electronic states of molecules inside living cells or tissues.

OCIS codes: (300.6420) Spectroscopy, nonlinear; (190.4180) Multiphoton processes.

References and links

1. P. J. Campagnola, A. C. Millard, M. Terasaki, P. E. Hoppe, C. J. Malone, and W. A. Mohler, "Three-Dimensional High-Resolution Second-Harmonic Generation Imaging of Endogenous Structural Proteins in Biological Tissues," Biophys. J. **82**(1), 493–508 (2002).
2. P. J. Campagnola and L. M. Loew, "Second-harmonic imaging microscopy for visualizing biomolecular arrays in cells, tissues and organisms," Nat. Biotechnol. **21**(11), 1356–1360 (2003).
3. D. A. Dombeck, K. A. Kasischke, H. D. Vishwasrao, M. Ingelsson, B. T. Hyman, and W. W. Webb, "Uniform polarity microtubule assemblies imaged in native brain tissue by second-harmonic generation microscopy," Proc. Natl. Acad. Sci. U.S.A. **100**(12), 7081–7086 (2003).
4. S. V. Plotnikov, A. C. Millard, P. J. Campagnola, and W. A. Mohler, "Characterization of the Myosin-Based Source for Second-Harmonic Generation from Muscle Sarcomeres," Biophys. J. **90**(2), 693–703 (2006).
5. A. Zoumi, A. Yeh, and B. J. Tromberg, "Imaging cells and extracellular matrix in vivo by using second-harmonic generation and two-photon excited fluorescence," Proc. Natl. Acad. Sci. U.S.A. **99**(17), 11014–11019 (2002).
6. E. Brown, T. McKee, E. diTomaso, A. Pluen, B. Seed, Y. Boucher, and R. K. Jain, "Dynamic imaging of collagen and its modulation in tumors in vivo using second-harmonic generation," Nat. Med. **9**(6), 796–801 (2003).
7. Y. Barad, H. Eisenberg, M. Horowitz, and Y. Silberberg, "Nonlinear scanning laser microscopy by third harmonic generation," Appl. Phys. Lett. **70**(8), 922–924 (1997).
8. D. Yelin and Y. Silberberg, "Laser scanning third-harmonic-generation microscopy in biology," Opt. Express **5**(8), 169–175 (1999).
9. D. Débarre, W. Supatto, A. M. Pena, A. Fabre, T. Tordjmann, L. Combettes, M. C. Schanne-Klein, and E. Beaurepaire, "Imaging lipid bodies in cells and tissues using third-harmonic generation microscopy," Nat. Methods **3**(1), 47–53 (2006).
10. L. Canioni, S. Rivet, L. Sarger, R. Barille, P. Vacher, and P. Voisin, "Imaging of Ca^{2+} intracellular dynamics with a third-harmonic generation microscope," Opt. Lett. **26**(8), 515–517 (2001).
11. C.-H. Yu, S.-P. Tai, C.-T. Kung, W.-J. Lee, Y.-F. Chan, H.-L. Liu, J.-Y. Lyu, and C.-K. Sun, "Molecular third-harmonic-generation microscopy through resonance enhancement with absorbing dye," Opt. Lett. **33**(4), 387–389 (2008).
12. C.-F. Chang, C.-H. Yu, and C.-K. Sun, "Multi-photon resonance enhancement of third harmonic generation in human oxyhemoglobin and deoxyhemoglobin," J. Biophotonics **3**(10-11), 678–685 (2010).

#203783 - $15.00 USD Received 26 Dec 2013; accepted 14 Apr 2014; published 23 Apr 2014

13. G. Veres, S. Matsumoto, Y. Nabekawa, and K. Midorikawa, "Enhancement of third-harmonic generation in absorbing media," Appl. Phys. Lett. **81**(20), 3714–3716 (2002).
14. A. Mathy, K. Ueberhofen, R. Schenk, H. Gregorius, R. Garay, K. Müllen, and C. Bubeck, "Third-harmonic-generation spectroscopy of poly(p-phenylenevinylene): A comparison with oligomers and scaling laws for conjugated polymers," Phys. Rev. B Condens. Matter **53**(8), 4367–4376 (1996).
15. G. O. Clay, A. C. Millard, C. B. Schaffer, J. Aus-der-Au, P. S. Tsai, J. A. Squier, and D. Kleinfeld, "Spectroscopy of third-harmonic generation: evidence for resonances in model compounds and ligated hemoglobin," J. Opt. Soc. Am. B **23**(5), 932–950 (2006).
16. R. D. Schaller, J. C. Johnson, and R. J. Saykally, "Nonlinear Chemical Imaging Microscopy: Near-Field Third Harmonic Generation Imaging of Human Red Blood Cells," Anal. Chem. **72**(21), 5361–5364 (2000).
17. H. Segawa, M. Okuno, H. Kano, P. Leproux, V. Couderc, and H.-O. Hamaguchi, "Label-free tetra-modal molecular imaging of living cells with CARS, SHG, THG and TSFG (coherent anti-Stokes Raman scattering, second harmonic generation, third harmonic generation and third-order sum frequency generation)," Opt. Express **20**(9), 9551–9557 (2012).
18. L. Gebicka and E. Banasiak, "Flavonoids as reductants of ferryl hemoglobin," Acta Biochim. Pol. **56**(3), 509–513 (2009).
19. R. Benesch, R. E. Benesch, and G. MacDuff, "Spectra of Deoxygenated Hemoglobin in the Soret Region," Science **144**(3614), 68–69 (1964).
20. N. Fukutake, "Comparison of image-formation properties of coherent nonlinear microscopy by means of double-sided Feynman diagrams," J. Opt. Soc. Am. B **30**(10), 2665–2675 (2013).
21. T. Wilson and C. Sheppard, *Theory and Practice of Scanning Optical Microscopy* (Academic, 1984).

1. Introduction

Various nonlinear optical processes have been recently applied to imaging of biological systems such as living cells and tissues [1–10]. Each nonlinear optical process provides unique capability of the contrast enhancement. Second harmonic generation (SHG) takes place only from non-centrosymmetric structures. SHG microscopy of fibril objects such as myosin filaments [1,2], microtubules [3,4] and collagen fibrils [5,6] is thus achieved with high sensitivity. Third harmonic generation (THG) is also widely used for microscopy [7,8], which is capable of imaging optical interfaces and inhomogeneity. Visualization of lipid droplets and the dynamics of Ca^{2+} ion flux inside a cell using THG microscopy have been reported [9,10].

The THG signal can be enhanced by electronic resonance effect [11–16]. In order to examine the resonance enhancement, however, we need to scan the excitation laser wavelength or to use spectrally broad laser source. Recently, we have developed multimodal nonlinear spectral imaging with third-order sum frequency generation (TSFG) [17]. TSFG is one of the third-order nonlinear optical processes [Fig. 1]. Similar to the THG process, the output photon energy of TSFG corresponds to the sum of the three input photon energies. If we use a white-light supercontinuum as an excitation light source, we can obtain multiplex TSFG spectra [17].

Although the contrast mechanism of the TSFG process is basically the same as that of THG, wavelength multiplexity of TSFG can provide spectral information on the electronic state of the sample molecule. In the present study, we investigated an electronic resonance effect on TSFG. As shown in Fig. 1, three intermediate states possibly contribute to the resonant TSFG process. If the photon energy of the incident laser light is close to that of the electronic state of the target molecule, TSFG is considered to be resonantly enhanced. Based on the spectral analysis of the multiplex TSFG spectrum, we can elicit the electronic resonance states of the target molecule. Furthermore, this technique can be easily implemented in electronically resonant TSFG imaging of molecules inside living cells.

We measured some hemoproteins to perform the proof-of-principle experiment. First, electronically resonant enhancement on TSFG was confirmed by the measurement of cytochrome *c* (cyt *c*) solution. Next, multiplex TSFG spectra of reduced and oxidized hemoglobin (Hb) solutions were measured and the spectral difference was evaluated.

#203783 - $15.00 USD Received 26 Dec 2013; accepted 14 Apr 2014; published 23 Apr 2014

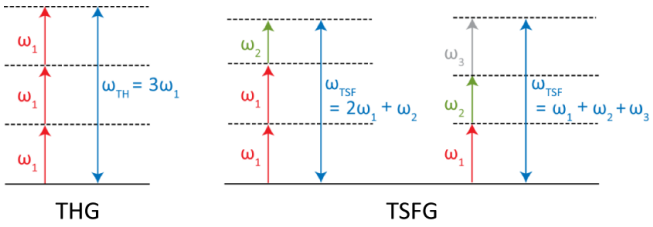

Fig. 1. Schematic diagrams of THG and TSFG.

2. Experimental

2.1 Samples

Samples were prepared as bulk solutions of hemoproteins. The solvent was phosphate buffered saline; PBS (gibco). First we measured Cytochrome *c* from bovine heart (Sigma Aldrich Japan) dissolved in PBS with 30 mg/mL concentration. Figure 2(a) shows the absorption spectrum of cyt *c* solution measured by a UV-vis spectrophotometer (HITACHI, U-4100). Second, we prepared oxidized and reduced hemoglobin solutions. Hemoglobin human lyophilized powder (Sigma Aldrich Japan) and Hemoglobin A_0, Ferrous Stabilized human (Sigma Aldrich Japan) were dissolved into PBS deaerated with nitrogen gas. Since the lyophilized powder was exposed to atmosphere, it was expected to be oxidized. Absorption spectra of these two solutions are shown in Fig. 2(b). The peak position of the absorption band of the lyophilized powder sample solution (orange) is 405 nm and that of the ferrous stabilized sample solution (green) is 414 nm. These peak positions are close to those of the oxidized and reduced Hbs [18,19]. We can therefore assign that the lyophilized powder sample and the ferrous stabilized sample were oxidized and reduced Hbs, respectively. The concentration of each solution was 16 mg/mL (oxidized) and 20 mg/mL (reduced). We prepared albumin solution with 11 mg/mL concentration for a control experiment.

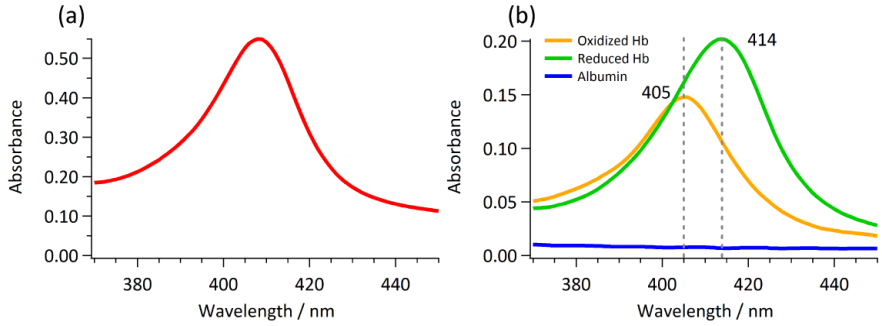

Fig. 2. Absorption spectra of sample solutions. (a) Absorption spectrum of cyt *c* dissolved into PBS. (b) Absorption spectra of two Hbs and albumin. Orange one is the spectrum of lyophilized powder sample solution, green corresponds to hemoglobin A_0, Ferrous Stabilized human. The blue spectrum corresponds to albumin solution.

2.2 Optical setup

The experimental setup is shown in Fig. 3(a), and described in detail elsewhere [17]. Briefly, the light source is a Q-switched microchip Nd:YAG laser. The fundamental 1064-nm radiation is firstly divided into two. One is used as an excitation light (ω_1). The other is introduced into a photonic crystal fiber, and is converted into a white-light supercontinuum. It is used as the other excitation light (ω_2). Under this condition, the possible combination for the TSFG process is $2\omega_1 + \omega_2$ and $\omega_1 + \omega_2 + \omega_2$'. After eliminating visible spectral components from the white-light continuum by a long-pass filter, two radiations are superimposed and introduced into a modified inverted microscope (Nikon: ECLIPSE Ti).

#203783 - $15.00 USD Received 26 Dec 2013; accepted 14 Apr 2014; published 23 Apr 2014

Excitation laser pulses are focused by an objective (Nikon: 40x / NA 0.9). TSFG signals are collected by the second objective lens (Nikon: 40x / NA 0.6), and introduced into a spectrograph (Princeton Instruments: SpectraPro300i). Multiplex TSFG spectrum is detected by a CCD camera (Princeton Instruments: PIXIS 100BR eXcelon) after eliminating excitation radiations. The laser power at the focus is 10 mW (ω_1) and 15 mW (ω_2), respectively. The sample is placed upon a piezo electric stage (Mad City Lab: Nano-LP200). For the measurement of the TSFG signals from interfaces, the sample is scanned in the axial direction. The total acquisition time is about 30 minutes per each sample.

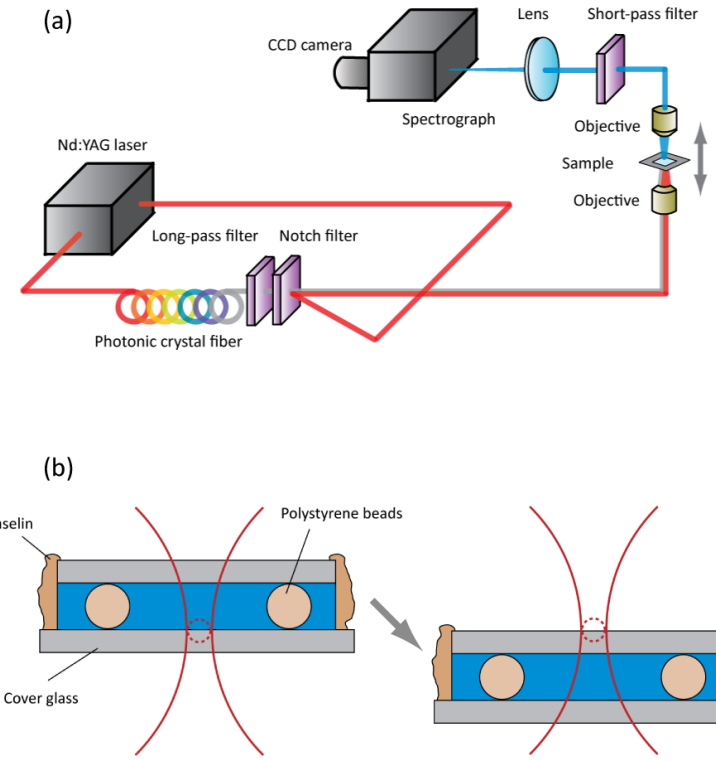

Fig. 3. Experimental setup: (a) TSFG miscrocpectroscopic system. (b) Schematics at the sample position. To obtain TSFG signal from interfaces, the preparation placed on the piezo electric stage was scanned in z, axial direction.

2.3 Sample preparation

TSFG takes place efficiently only at optically inhomogeneous areas such as interfaces under tight-focusing of the laser irradiation. In order to obtain multiplex TSFG spectrum from the hemoprotein solutions, we prepared the sample as shown in Fig. 3(b). The sample solution and 20-μm polystyrene beads (Polyscience) were co-sandwiched by two cover glasses. These beads functioned as spacers. The sample was scanned in the axial direction as shown in Fig. 3(b). As a result, TSFG signals from the bottom and upper glass/solution interfaces and the glass/air interface were detected.

2.4 Spectral analysis

In order to investigate the electronic resonance effect in multiplex TSFG spectra, we have analyzed obtained data in the following procedure. First, we obtained TSFG spectra of the sample at *bulk a*/*bulk b* interface ($I_{a/b}$). For the determination of the signal at the interface, the intensity of TSFG signal was plotted along the axial direction as shown in Fig. 4(b). The peak position should correspond to the center position of the interface. In order to take account of

#203783 - $15.00 USD Received 26 Dec 2013; accepted 14 Apr 2014; published 23 Apr 2014

the aberration originated from the tight-focusing condition, the multiplex TSFG spectrum was averaged over the interface within ± 2 μm. The averaged spectrum is denoted as the multiplex TSFG spectrum at *bulk a*/*bulk b* interface, $I_{a/b}$. Second, the TSFG spectrum at the upper glass/solution interface was used as the sample spectrum, and was divided with that at the glass/air interface as a reference spectrum in order to obtain intensity-corrected spectra. It should be noted that the TSFG spectrum at the bottom glass/solution interface is not appropriate for being used as the sample spectrum because re-absorption of the sample possibly takes place. Third, TSFG ratio spectrum was calculated by dividing the corrected TSFG spectrum of the sample with that obtained with buffer solution (PBS) prepared by the same procedure as the sample solution.

3. Results and discussion

3.1 Multiplex TSFG ratio spectrum of cyt c

Figure 4(a) shows a cross-sectional TSFG image of the buffer solution sandwiched with two cover glasses. As pointed out above, multiplex TSFG signals were obtained only at the interfaces. From the top part in Fig. 4(a), each dark layer corresponds to the surrounding air, an upper cover glass, the sample solution and a bottom cover glass. Due to polystyrene beads in a solution, TSFG signals from the upper and the bottom glass/solution interfaces were separately detected (see Fig. 4(b) and inset). Multiplex TSFG spectra obtained from the upper glass/solution interfaces of PBS (purple) and cyt *c* solution (red) were shown in Fig. 4(c). It is difficult to extract any noticeable difference between these two spectra. Based on the calculation described in the experimental section, we calculated the intensity-corrected TSFG spectra, indicated in Fig. 4(d). For comparison, the absorption spectrum of cyt *c* solution is also indicated in the same figure. As clearly observed, the intensity-corrected TSFG of cyt *c* solution gives large signal intensity around 400 nm, which is close to the absorption peak of the cyt *c* solution. This feature is not observed in the corrected TSFG spectrum of PBS. Although there should be no electronic resonance of PBS, the TSFG spectral profile of PBS is not spectrally flat. This is possibly because of the aberration under tight-focusing condition, which cannot be perfectly corrected by $I_{glass/air}$. In order to normalize the spectral profile, and extract information on electronic resonance effect, we calculated the TSFG ratio spectrum by dividing the intensity-corrected TSFG spectrum of cyt *c* solution by that of PBS. The resultant TSFG ratio spectrum in Fig. 4(e) clearly shows that the electronic resonant enhancement takes place due to the electronic state of cyt *c*.

#203783 - $15.00 USD Received 26 Dec 2013; accepted 14 Apr 2014; published 23 Apr 2014

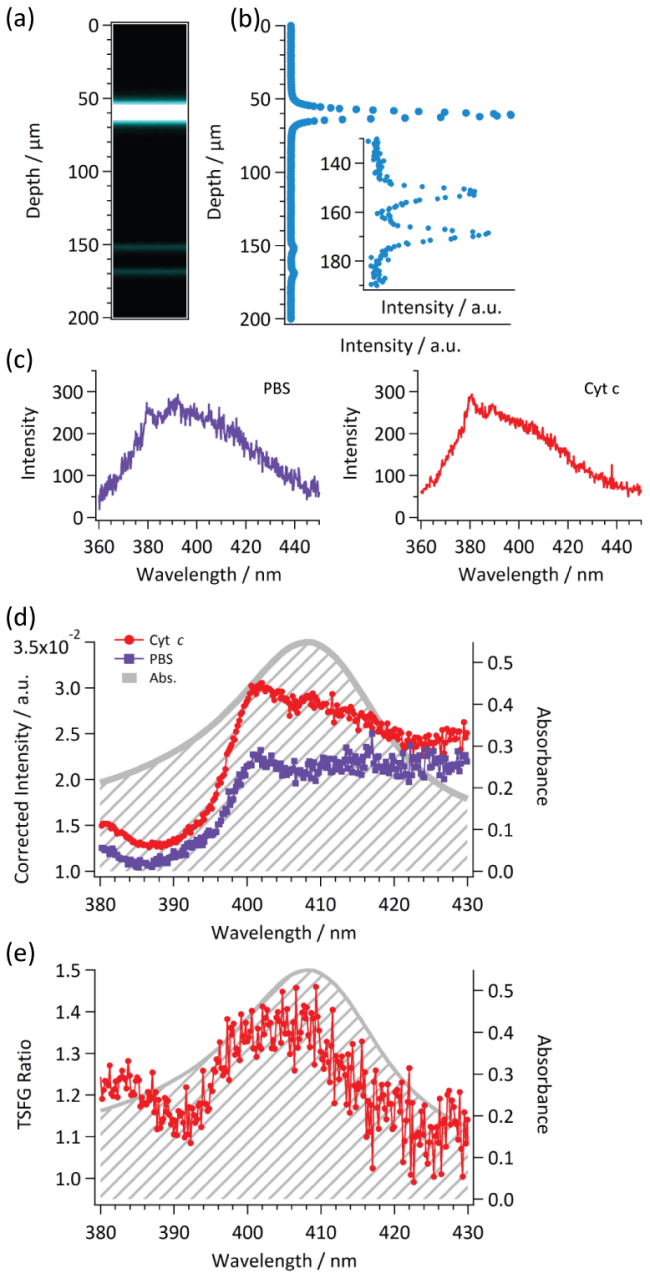

Fig. 4. Results of cyt *c* solution. (a) Cross-sectional image of TSFG. (b) Intensity profile of the axial direction scanning. The inset is the enlarged view of this profile. (c) TSFG spectra from the upper glass/solution interface. Left and right curves correspond to the averaged spectra of PBS (purple) and cyt *c* (red). (d) Corrected TSFG spectra of PBS (purple) and cyt *c* (red). For comparison, the absorption spectrum of cyt *c* solution is also shown. (e) Calculated ratio spectrum obtained by dividing the corrected TSFG spectrum of cyt *c* solution by that of PBS.

3.2 Multiplex TSFG ratio spectrum of Hb

Next we measured multiplex TSFG spectra of oxidized Hb, reduced Hb and albumin solutions. The intensity-corrected TSFG spectra are shown in Fig. 5(a). In comparison with the TSFG spectra of PBS (purple) and albumin solution (blue), those of oxidized Hb (orange)

#203783 - $15.00 USD Received 26 Dec 2013; accepted 14 Apr 2014; published 23 Apr 2014

and reduced Hb (green) show characteristic spectral profile around 400 nm, which corresponds to peak positions of the absorption bands of Hbs. The degree of enhancement is in the same order with that of the electronic resonant THG reported in the previous study [12]. In order to investigate the resonance effect in detail, we calculated the TSFG ratio spectra of Hbs [Fig. 5(b)]. TSFG ratio spectrum of reduced Hb shows the resonance enhancement in the wavelength region longer than that of oxidized Hb. This tendency is the same with that of absorption spectra of reduced and oxidized Hbs. It was thus verified that electronically resonant multiplex TSFG was capable of elucidating the electronic state of molecules.

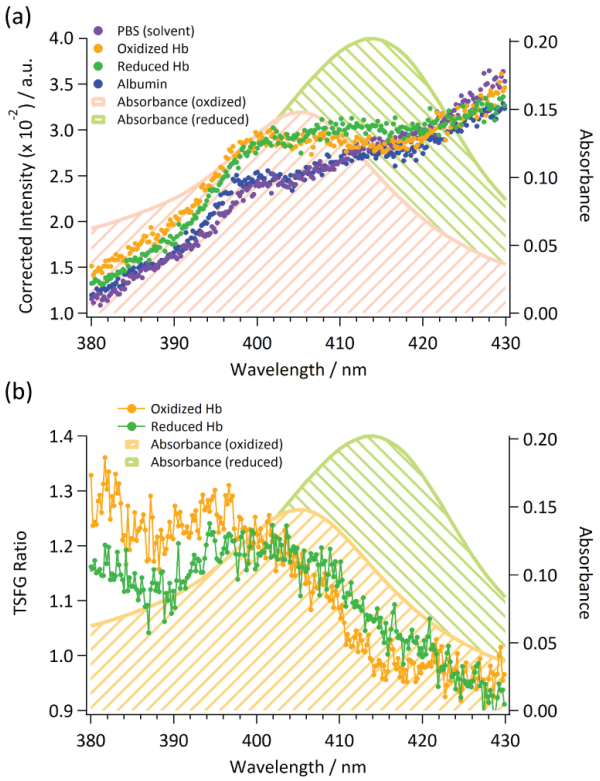

Fig. 5. (a) Intensity-corrected TSFG spectra of Hb solutions. Each plot corresponds to PBS (purple), oxidized Hb (orange), reduced Hb (green) and albumin (blue), respectively. For comparison, absorption spectra of oxidized and reduced Hb solutions are shown by solid lines. (b) Calculated ratio spectra of oxidized (orange) and reduced (green) Hb solutions.

3.3 Discussions

Both the ratio spectra of electronically resonant TSFG shown in Figs. 4(e) and 5(b) showed maxima at the wavelength shorter than those of the absorption peaks. Moreover, these spectral profiles show slightly dispersive lineshape. These features could be explained in the following by the spectral interference between resonant and nonresonant terms.

The observed signal is described by the third-order nonlinear optical susceptibility as follows,

$$\chi^{(3)}_{TSFG} = \chi^{(3)}_{resonant} + \chi^{(3)}_{nonresonant}. \quad (1)$$

Each term in Eq. (1) is described as,

#203783 - $15.00 USD Received 26 Dec 2013; accepted 14 Apr 2014; published 23 Apr 2014

$$\chi^{(3)}_{resonant} = \frac{A_{res}}{\omega_{res} - \omega_{TSFG} - i\Gamma_{res}}, \tag{2}$$

$$\chi^{(3)}_{nonresonant} = Ce^{i\theta}, \tag{3}$$

where A_{res} is the amplitude of the resonant component, ω_{TSFG} is the angular frequency of TSFG, ω_{res} is the resonance angular frequency and Γ_{res} is the damping rate of the electronic state. Here we assume that a single electronic state contributes to the resonant signal. In Eq. (3) C is the nonresonant component and θ is the relative phase between the resonant and the nonresonant term. It should be emphasized that the relative phase θ plays an important role in determining spectral shapes of nonlinear signals. The spectral profile of multiplex TSFG is then described as,

$$I(\omega_{TSFG}) = \left| \frac{A_{res}}{\omega_{res} - \omega_{TSFG} - i\Gamma_{res}} + Ce^{i\theta} \right|^2. \tag{4}$$

In order to determine the value of θ, we need to investigate the generation process of the TSFG signal. For simplicity, we simulated the signal-buildup process of the THG signal instead of TSFG for the present optical setup. The detail is described in the appendix. Briefly, the TSFG signals before and after an interface show relative phase π. In the present study, resonant TSFG takes place only in solution, whereas the nonresonant signal is generated mainly from glass. Therefore the phase difference of resonant and nonresonant TSFG becomes π. As a result, θ in Eq. (4) also becomes π.

Based on this result, TSFG ratio spectra were numerically simulated. We substituted π into θ and each peak position of the absorption spectrum into ω_{res} in Eq. (4). Calculated and observed spectra are shown in Fig. 6. The ratio spectra well reproduce the experimental result. It should be noted that the dip around 390 nm is probably due to the change of the dominant optical process between $2\omega_1 + \omega_2$ and $\omega_1 + \omega_2 + \omega_2$'. The interference between resonant and nonresonant TSFG with relative phase π thus leads to the dispersive spectral shape, yielding the apparent blue-shift of the peal position.

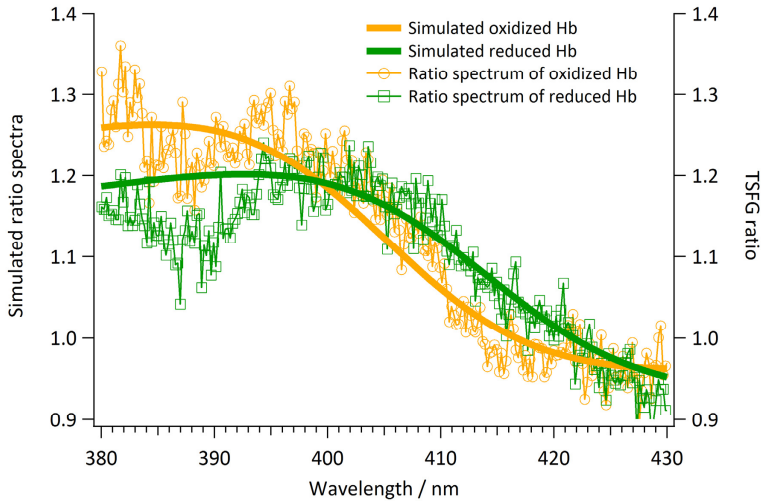

Fig. 6. Simulated TSFG ratio spectra of Hbs. In this calculation, ω_{res} of oxidized Hb is 405 nm, and that of reduced Hb is 414 nm, corresponding to peak positions of absorption spectra in Fig. 2(b). For comparison, the experimental results are also shown.

#203783 - $15.00 USD Received 26 Dec 2013; accepted 14 Apr 2014; published 23 Apr 2014

4. Conclusion

In this study, we detected the electronic resonant enhancement on TSFG process. The TSFG ratio spectrum of cyt *c* solution clearly showed the electronic resonance enhancement. This enhancement should reflect electronic state of cyt *c*. The TSFG ratio spectra of oxidized and reduced Hb solutions also indicated the electronic resonance effect. Both TSFG ratio and absorption spectra of reduced form showed the peak positions at the longer wavelength in comparison with those of oxidized form. The electronically resonant enhancement of TSFG was thus verified. Although the obtained TSFG ratio spectra showed spectral distortion, it was attributed to the interference of the resonant and nonresonant TSFG with relative phase π. Our method is thus capable of detecting information on the electronic state of molecules. Compared with confocal absorption microspectroscopy, our system has inherent three-dimensional sectioning capability due to the nonlinear optical process. Using this technique, we can develop an electronically resonant TSFG imaging system, which enables to study the electronic state of molecules inside biological samples such as living cells or tissues using near-infrared laser excitation. Taking into consideration the present intensity of signal, the typical exposure time is estimated to be 300 msec/pixel for a living mammalian cell using the white-light laser source in the present setup. It corresponds to 40 minutes acquisition for measuring a whole single cell. In order to improve the spectral and image acquisition time, the multi-focus or line scanning techniques should be exploited.

Appendix

We consider the confocal system which can be applied to our experimental apparatus. Details on the image-formation properties of the confocal system are described elsewhere [20]. For simplicity, we assume that the optical system does not have the aberrations. Hereafter, we use the coherent transfer function (CTF) to discuss the image-formation properties of nonlinear optical microscopy. CTF (f_x, f_y, f_z) is the Fourier transform of the amplitude point spread function (ASF) of the total system including the excitation and collection systems. In third-order nonlinear coherent microscopy, the ASF corresponds to the product of the cube of the excitation field formed by the excitation system and the signal field formed by the collection system [20]. The ASF is the image amplitude distribution of a single point object obtained by the total system. Therefore, the image amplitude formed from the object amplitude $\chi^{(3)}(x, y, z)$ through the nonlinear optical microscopy is expressed as,

$$A(x', y', z') = \int_{-\infty}^{\infty}\int_{-\infty}^{\infty}\int_{-\infty}^{\infty} \chi^{(3)}(x-x', y-y', z-z')\mathrm{ASF}(x, y, z)dxdydz, \qquad (5)$$

where the coordinate (x', y', z') indicates the sample-stage displacement, $\chi^{(3)}(x, y, z)$ corresponds to the nonlinear optical susceptibility distribution, and ASF (x, y, z) is the ASF [21]. The image intensity corresponds to the square of the modulus of the image amplitude.

First, we consider the semi-infinite slab defined by the following nonlinear optical susceptibility,

$$\chi^{(3)}_{\mathrm{step}}(x, y, z) = \chi^{(3)}_0 u(z) = \begin{cases} 0 & (z < 0) \\ \chi^{(3)}_0 & (z \geq 0) \end{cases}, \qquad (6)$$

where $u(z)$ represents the step function. The value of $\chi^{(3)}_0$ is dependent on the nonlinear optical process. We assume that the sample stage is scanned in z direction (direction of the optical axis), and the excitation and collection systems are unchanged, which means that the center of the ASF is fixed at a particular position (z = 0). The image amplitude of the semi-infinite slab (the complex amplitude of the signal for each depth position of the interface), $A_{\mathrm{step}}(z')$, is calculated as follows,

#203783 - $15.00 USD Received 26 Dec 2013; accepted 14 Apr 2014; published 23 Apr 2014

$$A_{\text{step}}(z') = \int_{-\infty}^{\infty}\int_{-\infty}^{\infty}\int_{-\infty}^{\infty}\chi^{(3)}_{\text{step}}(x-x', y-y', z-z')\text{ASF}(x, y, z)dxdydz = \chi^{(3)}_0 F(z') \tag{7}$$

with

$$F(z') = \int_{z'}^{\infty}\int_{-\infty}^{\infty}\int_{-\infty}^{\infty}\text{ASF}(x, y, z)dxdydz = \sum_{z=z'}^{\infty}\alpha(z)\Delta z \tag{8}$$

and

$$\alpha(z)\Delta z = \int_{z}^{z+\Delta z}\int_{-\infty}^{\infty}\int_{-\infty}^{\infty}\text{ASF}(x, y, z)dxdydz, \tag{9}$$

where z' represents the depth position of the interface relative to the center of the ASF. $F(z')$ is determined by the ASF and is independent of the nonlinear optical susceptibility. Using the formula of the Fourier transform, $F(z')$ is expressed as the inverse Fourier transform of the product of the CTF and $U(f_x, f_x, f_x)$, where

$$U(f_x, f_y, f_z) = \frac{1}{2}\delta(f_x)\delta(f_y)\left\{\delta(f_z) + \frac{i}{\pi f_z}\right\}, \tag{10}$$

which is the inverse Fourier transform of $u(z)$. Here $\delta(f)$ is the Dirac's delta function. Therefore, we obtain

$$\begin{aligned} F(z') &= \frac{1}{2}\int_{-\infty}^{\infty}\int_{-\infty}^{\infty}\int_{-\infty}^{\infty}\text{CTF}(f_x, f_y, f_z)\delta(f_x)\delta(f_y)\left\{\delta(f_z) + \frac{i}{\pi f_z}\right\} \\ &\quad \times\exp\left[i2\pi(f_x x' + f_y y' + f_z z')\right]df_x df_y df_z \\ &= \frac{1}{2}\int_{-\infty}^{\infty}\text{CTF}(0, 0, f_z)\left\{\delta(f_z) + \frac{i}{\pi f_z}\right\}\exp\left[i2\pi f_z z'\right]df. \end{aligned} \tag{11}$$

For later use, we also define the function $F'(z')$ as

$$F'(z') = \int_{-\infty}^{z'}\int_{-\infty}^{\infty}\int_{-\infty}^{\infty}\text{ASF}(x, y, z)dxdydz. \tag{12}$$

Likewise, $F'(z')$ is expressed as the inverse Fourier transform of the product of the CTF and $U'(f_x, f_x, f_x)$, where

$$U'(f_x, f_y, f_z) = \frac{1}{2}\delta(f_x)\delta(f_y)\left\{\delta(f_z) - \frac{i}{\pi f_z}\right\}. \tag{13}$$

which is the Fourier transform of $u(z)$. That is,

$$F'(z') = \frac{1}{2}\int_{-\infty}^{\infty}\text{CTF}(0, 0, f_z)\left\{\delta(f_z) - \frac{i}{\pi f_z}\right\}\exp\left[i2\pi f_z z'\right]df_z. \tag{14}$$

The value of $F(0)$ is particularly discussed below as a key factor for the coherent buildup of the signal in homogeneous medium. $F(0)$ is proportional to the complex amplitude of the signal in the case where the interface is located in the center of the ASF, and is given by

#203783 - $15.00 USD Received 26 Dec 2013; accepted 14 Apr 2014; published 23 Apr 2014

$$F(0)=\frac{1}{2}\int_{-\infty}^{\infty}\mathrm{CTF}(0,0,f_z)\left\{\delta(f_z)+\frac{i}{\pi f_z}\right\}df_z. \tag{15}$$

$F(0)$ is subject to $\mathrm{CTF}(0,0,f_z)$ which depends both on the nonlinear optical process and on the NAs of the excitation and collection systems [20].

Next, we consider the homogeneous medium. If the excitation beam is focused into the homogeneous medium with the nonlinear optical susceptibility of $\chi_0^{(3)}$, the signal amplitude A_{homo} is calculated as

$$\begin{aligned} A_{\mathrm{homo}} &= \chi_0^{(3)}\int_{-\infty}^{\infty}\int_{-\infty}^{\infty}\int_{-\infty}^{\infty}\mathrm{ASF}(x,y,z)dxdydz \\ &= \chi_0^{(3)}\left\{F(z')+F'(z')\right\} \\ &= \chi_0^{(3)}\left\{F(0)+F'(0)\right\} \\ &= \chi_0^{(3)}\left\{F(0)+F^*(0)\right\}. \end{aligned} \tag{16}$$

In the above equation, the relation of $\mathrm{ASF}(x,y,z)=\mathrm{ASF}^*(-x,-y,-z)$ was used. The factor $\cos\theta_{\mathrm{F}}$, where $\theta_{\mathrm{F}}=\mathrm{Arg}\left[F(0)\right]$, indicates the degree of coherent buildup and varies from 0 to 1. In particular, if $\cos\theta_{\mathrm{F}}=1$, the "constructive buildup" occurs. On the other hand, if $\cos\theta_{\mathrm{F}}=0$, the "destructive buildup" takes place, which means that the signal from each point in the ASF is canceled out.

The CTF of THG microscopy has an asymmetric profile; the value of $\mathrm{CTF}(0,0,f_z)$ becomes nonzero only in the positive f_z domain, and is zero in the negative f_z domain and at the origin [20]. This asymmetry of the CTF is connected to the distinguishing coherent buildup of the signal. Because the CTF is a positive real function, $F(0)$ for THG microscopy becomes a pure imaginary number with the asymmetry of the CTF mentioned above [Eq. (15)]. Consequently, the factor $\cos\theta_{\mathrm{F}}$ becomes zero ($\theta_{\mathrm{F}}=\pi/2$), which causes the destructive buildup. It is also shown by Eq. (16), in which the signals from the upper part $F(0)$ and the lower part $F^*(0)$ in the ASF are canceled out. In THG microscopy with a high-NA excitation system, irrespective of the NAs of the excitation and collection systems, the CTF has the asymmetric profile. As a result, the factor $\cos\theta_{\mathrm{F}}$ for THG microscopy is inevitably zero, which necessarily causes the destructive buildup regardless of the NAs. This destructive buildup corresponds to the well-known phase mismatch under THG microscopy.

In contrast, if the CTF is nearly symmetric around the origin and $\mathrm{CTF}(0,0,0)$ is non-zero, the imaginary part of $F(0)$ is canceled out and the real part remains [Eq. (15)]. In this case, $F(0)$ approaches a real number ($\cos\theta_{\mathrm{F}}\approx 0$). As a result, $F(0)+F^*(0)$ becomes a large value, leading to the constructive buildup of the signal [Eq. (16)]. This means that the large amount of the signal is generated from the homogeneous medium. For example, CARS microscopy exhibits the nearly-constructive buildup of the signal if the NAs of the excitation and collection systems are identical. In this case, the factor $\cos\theta_{\mathrm{F}}$ is nearly equal to 1 owing to the nearly-symmetric CTF. However, if the NA of the collection system is smaller than that of the excitation system in CARS microscopy, the CTF becomes asymmetric to some extent [20], which induces $\cos\theta_{\mathrm{F}}$ to be smaller than 1.

#203783 - $15.00 USD Received 26 Dec 2013; accepted 14 Apr 2014; published 23 Apr 2014

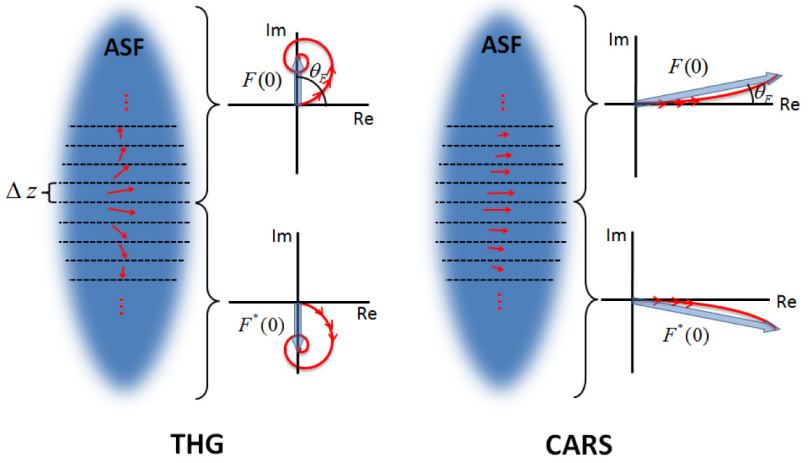

Fig. 7. Contribution of each section in ASF of THG (CARS) microscopy to the THG (CARS) signal. Arrows indicate complex numbers in complex plane. The summations of the contribution of each section for the upper and lower parts are shown.

Figure 7 illustrates how the signals of THG and CARS microscopy build up in the case where the excitation beam is focused into the homogeneous medium through a higher-NA excitation system than the collection system. In Fig. 7, the red arrows indicate the contributions of each section in the ASF to the total signals [Eq. (9)]. In THG microscopy, the phases of the signal from each section change rapidly, causing the destructive buildup. The sum of all arrows for THG microscopy in Fig. 7 reaches the imaginary axis (blue arrows); in other words, $F(0)$ for THG microscopy is a pure imaginary number ($\cos\theta_F = 0$). In contrast, in CARS microscopy, the phases of the signal from each section change slowly throughout the ASF, inducing $\mathrm{Re}[F(0)]$ to remain.

Figure 8 illustrates the destructive buildup of the THG signal, in which the contributions of the upper parts and lower parts from the ideal plane in the ASF are depicted. We assume that the depth position of the ideal plane is z'. Note that Fig. 8 is independent of the value of the nonlinear optical susceptibility which is a complex number in general depending on the electronically resonant condition. Since the function $\mathrm{CTF}(0,0,f_z)$ for THG microscopy has zero values in the negative f_z domain and at the origin, $F(z')$ [Eq. (11)] becomes

$$F_{\mathrm{THG}}(z') = \frac{1}{2}\int_0^\infty \frac{i}{\pi f_z}\mathrm{CTF}(0,0,f_z)\exp[i2\pi f_z z']df_z. \tag{17}$$

Likewise, $F'(z')$ for THG microscopy [Eq. (14)] becomes

$$F'_{\mathrm{THG}}(z') = -\frac{1}{2}\int_0^\infty \frac{i}{\pi f_z}\mathrm{CTF}(0,0,f_z)\exp[i2\pi f_z z']df_z. \tag{18}$$

Therefore, we obtain the relation of $F_{\mathrm{THG}}(z') = -F'_{\mathrm{THG}}(z')$. Thus, in the case of the homogeneous medium, the contributions of the upper part $F_{\mathrm{THG}}(z')$ and lower part $F'_{\mathrm{THG}}(z')$ from the ideal plane differ by π in phase regardless of the position of the ideal plane, resulting in the disappearance of the THG signal. This implies that θ in Eq. (4) is π .

#203783 - $15.00 USD Received 26 Dec 2013; accepted 14 Apr 2014; published 23 Apr 2014

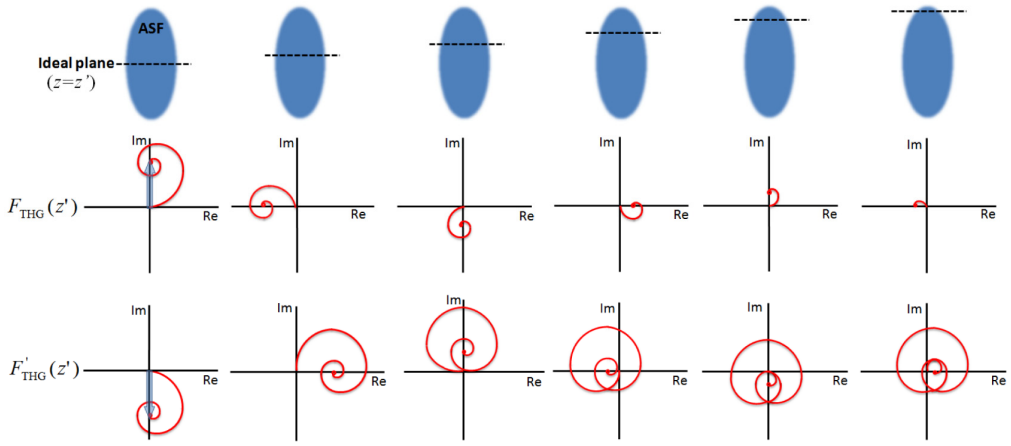

Fig. 8. Schematic of destructive buildup of THG signal. The top figures illustrate the ASFs of THG microscopy and the ideal planes. The middle figures describe the buildup of THG signal generated from the part above the ideal plane, representing the sum of the THG complex amplitudes that correspond to the arrows in Fig. 7. The bottom figures depict the buildup of THG signal generated from the part below the ideal plane. The leftmost figures show the case where the ideal plane is located in the center of the ASF.

In the case of the semi-infinite slab, THG microscopy visualizes only the interface. Figure 9 shows the image amplitude of the semi-infinite slab, which is proportional to $F_{\mathrm{THG}}(z')$, and the image intensity, which is proportional to $\left|F_{\mathrm{THG}}(z')\right|^2$. In Fig. 9, the curves of $\mathrm{Re}\left[F_{\mathrm{THG}}(z')\right]$, $\mathrm{Im}\left[F_{\mathrm{THG}}(z')\right]$, and $\left|F_{\mathrm{THG}}(z')\right|^2$ are plotted. The figures in the middle row of Fig. 8 correspond to the curves on the right side from the dashed line in Fig. 9.

In the present study, the resonant THG signal is generated only from the sample solution. Although the nonresonant THG signal is generated from both the solution and the glass, the nonresonant signal from the glass is more intense than that from the solution. Moreover, the phases of the nonresonant signals from the glass and the solution differ by π. Consequently, the total THG nonresonant signal has the identical phase with the nonresonant THG signal from the glass. Thus, the phase difference between the resonant THG signal and the nonresonant THG signal is inevitably π regardless of the position of the interface between the solution and the glass ($\theta = \pi$).

#203783 - $15.00 USD Received 26 Dec 2013; accepted 14 Apr 2014; published 23 Apr 2014

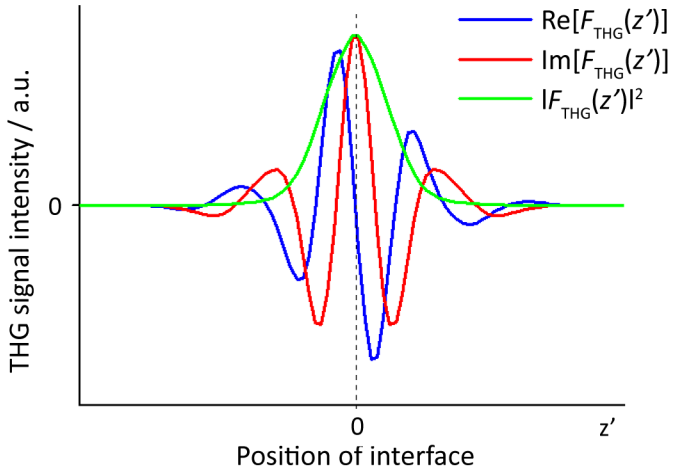

Fig. 9. The THG intensity and the THG complex amplitude acquired by scanning the interface in z direction.

Acknowledgments

This work is supported by JSPS-MESR-MAEE bilateral joint research project (SAKURA program) and The NOVARTIS Foundation (Japan) for the Promotion of Science. The authors thank the LEUKOS company for technical support with the dual-output supercontinuum light source. The authors gratefully acknowledge J. Ukon, UKON CRAFT SCIENCE, Ltd. for assisting with a fruitful collaboration between Japanese and French labs.